AZBA: A 3D Adult Zebrafish Brain Atlas for the Digital Age

Justin W. Kenney[1,2,*,§], Patrick E. Steadman[2,*], Olivia Young[1], Meng Ting Shi[1], Maris Polanco[1], Saba Dubaishi[1], Kristopher Covert[1], Thomas Mueller[3], and Paul W. Frankland[2,4-6,§]

[1]Department of Biological Sciences, Wayne State University, Detroit, MI, 48202, USA.
[2]Program in Neurosciences and Mental Health, The Hospital for Sick Children, Toronto, ON, M5G 1X8, Canada.
[3]Division of Biology, Kansas State University, Manhattan, KS, 66506, USA.
[4]Department of Physiology, University of Toronto, Toronto, ON, M5S 1A8, Canada
[5]Institute of Medical Sciences, University of Toronto, Toronto, ON, M5S 1A8, Canada
[6]Department of Psychology, University of Toronto, Toronto, ON, M5S 1A8, Canada
[*]These authors contributed equally to this work
[§]Corresponding authors

Abstract

Zebrafish have made significant contributions to our understanding of the vertebrate brain and the neural basis of behavior, earning a place as one of the most widely used model organisms in neuroscience. Their appeal arises from the marriage of low cost, early life transparency, and ease of genetic manipulation with a behavioral repertoire that becomes more sophisticated as animals transition from larvae to adults. To further enhance the use of adult zebrafish, we created the first fully segmented three-dimensional digital adult zebrafish brain atlas (AZBA). AZBA was built by combining tissue clearing, light-sheet fluorescence microscopy, and three-dimensional image registration of nuclear and antibody stains. These images were used to guide segmentation of the atlas into over 200 neuroanatomical regions comprising the entirety of the adult zebrafish brain. As an open source, online (azba.wayne.edu), updatable digital resource, AZBA will significantly enhance the use of adult zebrafish in furthering our understanding of vertebrate brain function in both health and disease.

Introduction

Uncovering general principles of neuroanatomical function and brain-behavior relationships requires the integration of findings across model organisms that range in complexity, organization, and accessibility (Brenowitz and Zakon, 2015; Marder, 2002; Yartsev, 2017). Amongst vertebrate model organisms in neuroscience, zebrafish are relative newcomers that have grown in popularity in recent years (Kenney, 2020; Orger and de Polavieja, 2017). Originally established as a model organism for developmental biology due to ease of domestication, high fecundity, and early life transparency (Parichy, 2015), the increased popularity of zebrafish is driven by recent advancements in brain imaging, molecular genetic manipulation, and behavior. To further enhance the use of zebrafish as an animal model in neuroscience, we created a digital three-dimensional brain atlas (AZBA: adult zebrafish brain atlas). Although several digital atlases exist for larval zebrafish (Kunst et al., 2019; Randlett et al., 2015; Ronneberger et al., 2012; Tabor et al., 2019), no atlas of equivalent detail has been created for adult zebrafish. Adult zebrafish provide several important advantages over larval zebrafish such as a mature and histologically differentiated neuroanatomy and a rich behavioral repertoire that includes long-term associative memory, complex social interactions, and goal-driven behaviors (Gerlai, 2016; Kalueff et al., 2013; Kenney et al., 2017; Nakajo et al., 2020).

Three-dimensional digital brain atlases are essential tools for modern neuroscience because they facilitate lines of inquiry that are not possible with two-dimensional book-based atlases. For example, visualization of the three-dimensional structure of the brain and incorporation of new data or discoveries are difficult, if not impossible, with a print atlas. In contrast, digital atlases enable exploration of brain structures in any arbitrary three-dimensional perspective and can be readily updated to incorporate new information such as patterns of gene expression and anatomical connectivity, as has been done for the mouse (Wang et al., 2020). Such features are important for fields like neurodevelopment and comparative neuroanatomy

that rely on three-dimensional topologies to understand how specific brain regions develop and relate across species. A digital atlas would also enhance the use of adult zebrafish in disease modeling by enabling a more comprehensive understanding of how the brain changes in response to insults that occur in neurodevelopmental disorders (Sakai et al., 2018), traumatic brain injury (McCutcheon et al., 2017), neurodegeneration (Xi et al., 2011) and the formation and spreading of gliomas (Idilli et al., 2017). Finally, digital atlases enable automated segmentation of new images, which is essential for whole brain mapping approaches that can lead to unexpected discoveries of regional function (Bahl and Engert, 2020; Kim et al., 2015; Pantoja et al., 2020; Randlett et al., 2019). Whole brain activity mapping also facilitates powerful network approaches to understanding brain (Bassett and Sporns, 2017; Coelho et al., 2018; Vetere et al., 2017; Wheeler et al., 2013), yielding insight into how coordinated brain-wide activity gives rise to behavior.

The generation of an adult zebrafish brain atlas presents several challenges in comparison to the larval brain because the mature brain is opaque and an order of magnitude larger; this makes traditional whole mount approaches impossible and confocal or wide-field microscopy infeasible. We overcome these roadblocks by exploiting recent developments in histology and microscopy. To enable whole-mount imaging, we rendered adult brains transparent using a tissue clearing approach (iDISCO+) that is compatible with different stains such as small molecules, antibodies, and *in situ* probes (Kramer et al., 2018; Renier et al., 2016). High resolution imaging of samples as large as intact adult brains is not amenable to conventional microscopic techniques, so we turned to light-sheet fluorescence microscopy for rapid large volume imaging with minimal photobleaching (Pitrone et al., 2013; Reynaud et al., 2014). To generate an atlas that minimizes individual variations in neuroanatomy, we registered three-dimensional volumes from multiple animals into the same anatomical space prior to averaging (Lerch et al., 2011). To help guide segmentation and generate insight into the

neurochemical organization of the brain, images from ten different antibody stains were also registered into the same anatomical space. Finally, we performed manual segmentation, delineating the atlas into over 200 neuroanatomical regions, including nuclei and white matter tracts.

Taken together, AZBA is the most comprehensive, detailed, and up to date atlas of the adult zebrafish brain. We have made all averaged images freely available (https://doi.org/10.5061/dryad.dfn2z351g; azba.wayne.edu) to enable their use in exploring the organization of the zebrafish brain and automated segmentation for activity mapping. By generating this resource using readily available techniques, AZBA can be continuously updated to reflect the latest findings in zebrafish neuroanatomy. We anticipate this becoming an indispensable resource as adult zebrafish continue to gain traction as a model organism in understanding the intricacies of the vertebrate brain.

Results

Overall Strategy

To create an averaged three-dimensional atlas, we developed a sample preparation and analysis pipeline for whole-mount 3D image acquisition and registration (Figure 1). We used a whole-mount preparation to avoid issues with slice-based techniques such as tissue loss, tearing, and distortion. To circumvent the challenge of tissue opacity, we used a rapid organic solvent based tissue clearing technique, iDISCO+ (Renier et al., 2016), that renders brains optically transparent. Because conventional microscopic techniques are not suitable for large volume imaging, we used light-sheet microscopy. Image stacks from individual fish brains were converted to 3D volumes and registered into the same anatomical space prior to averaging. Finally, average 3D images were manually segmented into their constituent brain regions.

Light-sheet Imaging

Tissue clearing using iDISCO+ resulted in transparent brains (Figure 2A). iDISCO+ is compatible with a variety of stains, such as a nuclear stain (TO-PRO), that allowed us to approximate the Nissl stain in the print atlas (Wulliman et al., 1996). Cleared and stained brains were imaged in the horizontal plane with an in-plane resolution of 3.25 μm and an axial step-size of 4 μm (Figure 2B) yielding near-isotropic signals at sufficient resolution to clearly distinguish regional boundaries. From this collection of images, we generated three-dimensional volumes (Figure 2C) that enabled viewing at any arbitrary angle including the coronal and sagittal planes (Figure 2D). Images were subject to quality-control so that those damaged during dissection were discarded. We retained seventeen sets of nuclear stained and associated autofluorescence images from both male and female fish (8 female), each of which were transformed into 3D volumes for registration.

153

154 *3D Image Registration*

155 The atlas was generated by registering images from individual animals into the same
156 space, thereby creating an anatomical average. This approach has been previously used in
157 humans (Klein et al., 2009), mice (Dorr et al., 2008; Steadman et al., 2014), macaques
158 (McLaren et al., 2009) and zebrafish larvae (Kunst et al., 2019; Randlett et al., 2015;
159 Ronneberger et al., 2012; Tabor et al., 2019). We used the contrast from the TO-PRO signal
160 and an image registration pipeline toolkit (Friedel et al., 2014) to perform iterative registration to
161 generate a consensus image (Figure 3). This method begins with a 6-parameter linear
162 registration to rotate and translate the initial image dataset followed by a 12-parameter affine
163 registration to scale, translate, rotate, and shear the dataset with a pair-wise approach to avoid
164 bias by outlier images (Figure 3A). Lastly, an iterative non-linear registration with 6 iterations at
165 subsequently higher resolutions was performed using minctracc (Collins and Evans, 1997). This
166 resulted in a set of linear and non-linear transformations for each TO-PRO image in our dataset
167 from native space to a consensus space and orientation. These transformations were then
168 applied to corresponding autofluorescence images, thereby creating an atlas with averaged
169 images containing TO-PRO and autofluorescence signals (Figure 3B).

170

171 *Antibody stains*

172 To provide additional guidance for segmentation and generate insight into the
173 neurochemical organization of the adult zebrafish brain, we also acquired images using ten
174 different antibody stains (Figure 4A and Table S1). We sought stains that would identify different
175 cell types in the brain, such as neurons (HuC/D), radial glial cells (glial fibrillary associated
176 protein; GFAP), and proliferating cells (proliferating cell nuclear antigen; PCNA), markers for

different neurotransmitters (tyrosine hydroxylase (TH), 5-hydroxytryptamine (5-HT), and choline acetyltransferase (ChAT)) and calcium binding proteins (parvalbumin (PV), calbindin, and calretinin). Some of these stains, such as TH, 5-HT, ChAT, and calretinin have already been subject to brain-wide analysis, making them useful for guiding segmentation.

Fully realizing the utility of different stains requires images to be brought into the same anatomical space as the previously generated TO-PRO average. To achieve this, during imaging of antibody stains we also acquired autofluorescence images, thereby providing a bridge between the antibody images and the TO-PRO images. Autofluorescence images from antibody stains were registered with the autofluorescence channel of the TO-PRO images, yielding a set of transformations that were used to bring antibody stains into the same anatomical space as the TO-PRO stain (Figure 4B). To generate a representative image for each antibody, we averaged together at least five independent brains. Our approach resulted in strong correspondence between antibody images and the TO-PRO stain (Figure 4C). The utility of this approach is apparent from examining structures known to express high levels of specific enzymes, like TH in the locus coeruleus (Figure 4D; green arrows).

Registration Precision

To compare registration precision using TO-PRO and autofluorescence signals we labelled six different landmarks in the atlas images and corresponding points in acquired images. Transforms derived from the registration process were then applied to the acquired image's labelled landmarks. We then measured the Euclidean distance between the transformed points and the points in the atlas. Using a mixed model ANOVA (2 × 16; signal (between subject) × landmark (within subject)), we found a main effect of signal ($F(1,13) = 1084$, $P = 6.6 \times 10^{-14}$) with the TO-PRO signal having greater mean precision (15 ± 10 μm vs 99 ± 53

201 μm; Figure S1). However, there was also a significant effect of landmark ($F(5,65) = 98$, $P < 2 \times$
202 10^{-16}), and an interaction between signal and landmark ($F(5, 65) = 120$, $P < 2 \times 10^{-16}$). A closer
203 examination of the data revealed that in the autofluorescence images the average precision of
204 each landmark covers a much wider range (17 to 180 μm) than TO-PRO (9 to 23 μm). In the
205 autofluorescence image, the landmark with the highest precision (point 5; 17 ± 4 μm) has
206 precision on par with the TO-PRO average. This suggests that the larger error measured using
207 autofluorescence images is most likely due to experimenter error in selecting points, reflecting
208 the paucity of well-defined landmarks in this signal compared to the richer, high contrast TO-
209 PRO images.

210

211 *Segmentation*

212 Registered images were used to segment the brain into its constituent parts (Figure 5;
213 see Table S2 for anatomical abbreviations and colors). Segmentation was primarily guided by
214 the seminal atlas of Wullimann and colleagues (1996). Regional boundaries and terminology
215 were updated for parts of the brain that have been subject to more recent analysis such as the
216 telencephalon, hypothalamic regions, and motor nuclei (Mueller et al., 2004; Porter and Mueller,
217 2020; Rink and Wullimann, 2001). Segmenting large, clearly delineated regions, such as the
218 optic tectum and the cerebellum, was straightforward (Figure 5A). Small nuclei that only appear
219 in one or two slices in the atlas or in images from only one axis proved more challenging. For
220 such regions, we primarily made use of the coronal axis due to it being the most extensively
221 represented in both the atlas and the literature (Figure 5A, bottom). The horizontal and sagittal
222 planes enabled us to identify the anterior-posterior boundaries (Figure 5A, top and middle). To
223 ensure we captured as many neuronal structures as possible, we also made extensive use of a
224 neuronal marker (HuC/D) in conjunction with the nuclear stain, which allowed us to safely
225 identify many boundaries (Figure S2A). Other challenges included the fact that the original brain

226 atlas contains a significant amount of unsegmented space. We labelled these regions as
227 “unknown” and according to their lowest anatomical level (e.g. unknown ventral telencephalon
228 (UnkVT), unknown diencephalon (UnkD), etc.). Explicitly labelling these regions distinguishes
229 them from the “clear” label that is used for areas outside the brain to facilitate computational
230 analysis using the atlas. Identification of tracts was largely based on a combination of
231 autofluorescence and lack nuclear and neuronal staining since we were unsuccessful in finding
232 a white matter stain compatible with iDISCO+ (e.g. the MLF: Figure 4D, pink arrowheads). We
233 anticipate future work will aid in filling these unsegmented regions with the potential to discover
234 new neuronal circuits and anatomical structures.

235 Segmentation was also guided by stains with antibodies that have been used in prior
236 studies of the adult zebrafish brain. This includes amines like TH and 5-HT (Kaslin and Panula,
237 2001; Rink and Wullimann, 2001), ChAT to identify cholinergic neurons and motor nuclei
238 (Mueller et al., 2004), and calcium binding proteins like calretinin (Castro et al., 2006a, 2006b).
239 All of our immunostainings showed high overlap with prior work, establishing the validity of
240 these antibodies (Figures 5B,C, and S1B,C). For example, in the telencephalon we found
241 extensive TH expression in the olfactory bulb (Figure 5B-a), and as a continuous band ventral to
242 the Dc region (Figure 5B-b). As previously reported, TH staining was also elevated in the optic
243 tectum, thalamic, and hypothalamic regions (Figure 5B-c,d), the LC (Figure 5B-e), and in the
244 XLo of the hindbrain (Figure 5B-f). We found 5-HT staining to be more diffuse in regions like the
245 optic tectum and the dorsal part of the telencephalon (Figure 5C-a,b), with pockets of high
246 expression restricted to regions like the PVO (Figure 5C-c), PTN (Figure 5C-d), posterior portion
247 of the Hc (Figure 5C-e), and the SR (Figure 5C-f). Using ChAT, we could clearly discern
248 staining in places such as the RT (Figure S2B-a), near the TTB (Figure S2B-b), and in the SRN
249 and NLV (Figure S2B-c). ChAT staining was also apparent in several motor nuclei such as the
250 OENr and VIIm (Figure S2B-d), OENc (Figure S2B-e), and IXm (Figure S2B-e). Finally,

examples of high levels of calretinin staining can be seen in the olfactory bulb (Figure S2C-a), the Dm (Figure S2C-b), the PSP and optic tract (Figure S2C-c), optic tectum (Figures S1C-c,d,e), the TLa, SG, TGN, and anterior portion of the DIL (Figure S2C-d) with particularly strong staining in the SGN (Figure S2C-e) and DON (Figure S2C-f).

Our segmentation resulted in a three-dimensional model of the zebrafish brain that can be viewed from any arbitrary angle (Figure 5D). Each nucleus, white matter tract, ventricle, and anatomical space was given a unique abbreviation and color, totaling 204 regions (Table S2) and associated with an anatomical hierarchy (Table S3, File S1). The full extent of the atlas can be appreciated using the website (azba.wayne.edu) or ITK-SNAP (Yushkevich et al., 2019), a freely available software package designed for viewing three-dimensional medical images that allows for the simultaneous viewing of the stains and segmentation in the coronal, sagittal, and horizontal planes (Figure 6). All files for exploring AZBA are freely available for use in ITK-SNAP or other programs (https://doi.org/10.5061/dryad.dfn2z351g).

Sex and brain volume

Because the goal of the atlas was to generate a representative brain, we combined images from both male and female fish. To determine if there was an effect of sex on brain volumes in our TO-PRO image set, we used a mixed model ANOVA (2 × 204; sex (between subjects) × brain region (within subjects)). We found neither an effect of sex ($F(1,15) = 0.11$, $P = 0.75$; Figure S3) nor an interaction between sex and brain region ($F(199, 2985) = 0.14$, $P = 1$; Figure S4) suggesting that sex did not affect the overall size of the brain or individual regions. We did find a main effect of region ($F(199, 2985) = 497$, $P < 2 \times 10^{-16}$), consistent with the wide range of region sizes observed across the brain (0.000026 to 0.53 mm^3; Table S3).

275 *Neurochemical organization of the adult zebrafish brain*

276 We used AZBA to generate insight into the neurochemical organization of the adult
277 zebrafish brain using antibody stains that have not previously been subject to brain-wide
278 examination. Parvalbumin (PV) is a calcium binding protein that labels a class of inhibitory
279 interneurons (Celio, 1986). We found several highly concentrated areas of PV staining such as
280 in the anterior portions of the olfactory bulb (Figure 7A), APN and DAO (Figure 7A-b), the TSc
281 (Figure 7A-c), the DON and VIII of the hindbrain (Figure 7A-f), and very high levels in the ventral
282 portion of the molecular layer of the cerebellum (Figure 7A-d,e) the latter of which likely
283 corresponding with Purkinje and crest cells (Bae et al., 2009).

284 Prox1 is a homeobox gene critical for regulating neuronal development with widespread
285 expression in larval fish. In juveniles and adult zebrafish, Prox1 expression decreases rapidly
286 and is eventually confined to relatively few regions (Ganz et al., 2012; Pistocchi et al., 2008). In
287 the adult zebrafish pallium, Prox1 was reported to be present in the neuronal layer of the Dl with
288 more diffuse staining in posterior portion of the Dc, which we also observed (Figure 7B-b). We
289 also observe high levels of Prox1 in the olfactory bulb (Figure 7B-a), the habenula (Figure 7B-
290 b), the Val and hypothalamus (Figure 7B-d), and the DIL and the molecular layer of the
291 cerebellum (Figure 7B-e,f).

292 PCNA is a marker for proliferating cells (Grandel et al., 2006; Wullimann and Puelles,
293 1999). Consistent with widespread neurogenesis in the adult zebrafish brain, we found PCNA
294 expressed in many neurogenic niches with the highest expression along the midline (Figure
295 7C). For example, in the telencephalon we noticed a band of high expression along the midline
296 in the ventral telencephalon that begins near the olfactory bulbs (Figure 7C-a) with a second
297 area in the posterior portion corresponding to the PPa (Figure 7C-b). We also saw high levels of
298 expression in parts of the thalamus (VM; Figure 7C-c), the hypothalamus (Hd and posterior

portion of Hc) and the valvula, caudal lobe, and molecular layers of the cerebellum (Figure 7C-d,e,f).

Calbindin is a calcium binding protein important for regulating intracellular signaling that is often used in comparative neurological studies (Schmidt, 2012). We found calbindin to be concentrated in the fiber layers of the olfactory bulbs (Figure S2D-a), the Dm in the telencephalon (Figure S2D-b), the VOT (Figure S2D-c), throughout the optic tectum (Figure S2D-c,d,e), the TLa (Figure S2D-d), SGN (Figure S2D-e), and in the VIII and DON of the hindbrain (Figure S2D-f). Notably, calbindin staining patterns largely overlapped with calretinin (Figure S2C).

GFAP is a marker for non-neuronal cells like astrocytes, radial glial cells, and ependymal cells (Doetsch et al., 1997; Eng et al., 2000). Accordingly, we found GFAP most concentrated near the midline and ventricles (Figure 7D). Pockets of expression were present that were not adjacent to ventricles such as near the entopeduncular nuclei (Figure 7D-a), the habenula and anterior portions of the thalamus (Figure 7D-b) and nuzzled between the NI and TSvl (Figure 7D-d). Throughout the hindbrain, GFAP expression was largely restricted to the edges of the brain with the exception of the IR and dorsolateral edge of the XLo (Figure 7D-e,f).

Discussion

In the present article, we introduce a new resource for the zebrafish community: AZBA, a three-dimensional adult zebrafish brain atlas that can be downloaded (https://doi.org/10.5061/dryad.dfn2z351g) or explored on the web (azba.wayne.edu). This resource will facilitate a wide variety of neurobiological studies using adult zebrafish aimed at dissecting neural circuits of behavior, understanding brain pathology, and discovering novel and conserved neuroanatomy. We created AZBA by leveraging advances in tissue clearing, light-sheet fluorescent microscopy, and image registration, resulting in the most detailed atlas for adult zebrafish to date. Tissue clearing allowed us to take a whole-mount approach, overcoming the natural opacity of the adult brain and issues associated with slice-based techniques such as tissue loss, tearing, and distortion. Laser fluorescence light-sheet microscopy was used to image the large volume of the zebrafish brain with high resolution and minimal photobleaching. Finally, we used three-dimensional image registration to create images derived from multiple animals and inclusion of ten antibody stains into the same anatomical space. These were then used to guide segmentation of the atlas into over 200 different neuroanatomical regions.

AZBA represents a significant departure from two prior adult zebrafish brain atlases. The seminal book atlas from Wullimann and colleagues (1996) is exceptionally detailed and has guided zebrafish neuroscience research for over two decades. However, being in print, it has not been updated with the latest findings and its two-dimensional visual presentation and lack of chemoarchitectural markers makes identifying regional boundaries across anatomical planes problematic. More recently, Ullmann and colleagues used magnetic resonance imaging (MRI) to create a three-dimensional atlas for adult zebrafish (Ullmann et al., 2010). Using a 16.4 Tesla magnet, they imaged a single brain at approximately 10 μm resolution and segmented it into 53 regions. Although an important achievement, MRI is limited in its ability to detect neurochemical markers and does not integrate easily with genetic labeling techniques. Furthermore, such

strong magnets are not readily available to most researchers. In contrast, by combining recent advances in widely available tissue clearing techniques, light-sheet microscopy, and image registration, AZBA is highly versatile, detailed, and accessible.

Antibody stains were central to developing AZBA because they validated our approach and improved segmentation through comparison to prior work. Indeed, patterns of our neurotransmitter related stains largely agree with previous reports probing TH (Castro et al., 2006b; Kaslin and Panula, 2001; Ma, 2003; Yamamoto et al., 2010), 5-HT (Kaslin and Panula, 2001; Norton et al., 2008), and ChAT (Castro et al., 2006b; Clemente et al., 2004; Mueller et al., 2004). PCNA also overlaps with earlier findings using both PCNA antibodies and bromoeoxyuridine labelling (Ampatzis et al., 2012; Byrd and Brunjes, 2001; Grandel et al., 2006; Ito et al., 2010; Makantasi and Dermon, 2014; von Krogh et al., 2010). Likewise, stains against the calcium binding proteins like calretinin, calbindin, and PV, largely overlap with prior work with only minor exceptions. Consistent with previous studies we find calretinin expressed in the olfactory bulb (Kress et al., 2015), telencephalon (Porter and Mueller, 2020) and posterior parts of the brain, with the only notable exceptions being our lack of staining in the torus semicircularis and perilemniscal nucleus (Castro et al., 2006b, 2006a). For calbindin, despite using the same antibody, we find that our staining in the telencephalon looks different than previous work (von Trotha et al., 2014) where we find little staining in the subpallium, and instead see staining in the medial zone of the dorsal telencephalon limited to its posterior extent. For PV, we also note significant overlap with prior work where we see labelling in cell bodies of the cerebellum and olfactory bulbs, but less consistency in the more diffuse staining in the telencephalon (Ampatzis and Dermon, 2007; Bae et al., 2009; Mueller et al., 2011; Porter and Mueller, 2020). Some of these minor discrepancies may be due to changes in antigenicity arising from the use of different methodologies for fixation, loss of sparse signal due to the averaging of multiple images, tissue distortion (Renier et al., 2016; Richardson and Lichtman,

375 2015), or because prior work reported images from single animals and may be more susceptible
376 to individual variation in expression patterns compared to the present work where images are
377 averaged across several subjects. Nonetheless, our high correspondence with the previous
378 literature suggests the present work accurately represents the adult zebrafish brain.

379 Of the antibody stains that had not been subject to extensive prior work, the findings of
380 greatest interest are from Prox1, a homeobox protein critical to the development of an array of
381 organs and cell types including neurons during embryonic and adult stages (Elsir et al., 2012;
382 Kaltezioti et al., 2010; Karalay et al., 2011). We found Prox1 staining in the telencephalon,
383 consistent with prior work (Ganz et al., 2012), as well as the habenula, parts of the
384 hypothalamus, and the cerebellum (Figure 7B). Hypothalamic *Prox1* expression in larval
385 zebrafish has been found to be important for the development of catecholaminergic neurons
386 (Pistocchi et al., 2008). However, we do not see overlap between TH and Prox1 in the
387 hypothalamus, suggesting Prox1 may be important for the development, but not the
388 maintenance, of hypothalamic catecholaminergic neurons. In adult mice, Prox1 is present in the
389 dentate gyrus of the hippocampus and GFAP positive cells localized to white matter tracts in the
390 cerebellum (Karalay et al., 2011; Lavado and Oliver, 2007). Interestingly, we find overlap
391 between Prox1 and GFAP in the olfactory bulb and the edges of the telencephalon, but not the
392 cerebellum, where Prox1 has greater overlap with PCNA, a marker for proliferating cells. The
393 dentate gyrus in mice is notable for being one of the few areas where adult neurogenesis has
394 been demonstrated (Ming and Song, 2011). Thus, the broader expression of Prox1 in our study
395 may reflect the presence of more widespread neurogenesis in adult zebrafish compared to mice
396 (Kizil et al., 2012).

397 We view the current segmentation and image collection that comprises AZBA as a first
398 version that will be continually updated. To facilitate updating, and encourage input from the
399 scientific community, we have created a website (azba.wayne.edu) where we invite comments

and suggestions for updates. In addition, we expect future work will incorporate more antibody images and *in situ* hybridization probes for understanding how patterns of protein and gene expression vary across the brain. Through collaboration with the zebrafish community, we plan to incorporate the wealth of Gal4 and Cre/loxP lines that have been generated to characterize expression patterns in the adult brain. We envision a process where scientists send fixed brain samples to a central lab for tissue clearing, imaging, and registration to the atlas for incorporation into our online resource. A similar approach has been taken with larval fish (Kawakami et al., 2010; Kunst et al., 2019; Randlett et al., 2015; Ronneberger et al., 2012; Tabor et al., 2019). However, images from adult animals are important because transgene expression patterns can change as animals mature (Lal et al., 2018).

AZBA also enables new insight into the functional organization of the zebrafish brain by facilitating whole-brain activity mapping as has been achieved with larval zebrafish (Ahrens et al., 2012; Randlett et al., 2015). New images can be automatically segmented into individual brain regions by registration to our averaged autofluorescence or nuclear stained images (Figure 4). Because adult zebrafish have a mature neuroanatomy and a larger behavioral repertoire than larval fish, this will provide an important new avenue for exploiting the power of the zebrafish model system to yield insight into the functional organization of the vertebrate brain and how it relates to behavior.

AZBA provides an unprecedented view of the adult zebrafish brain, consisting of averaged three-dimensional nuclear stained and antibody images registered into the same space. All files associated with the atlas are available to the community (https://doi.org/10.5061/dryad.dfn2z351g) and can be viewed online (azba.wayne.edu) or with ITK-SNAP, a freely available software package (Yushkevich et al., 2019). With AZBA, adult zebrafish join the ranks of other vertebrate model organisms in neuroscience that have highly detailed digital atlases such as larval zebrafish (Kunst et al., 2019; Randlett et al., 2015;

Ronneberger et al., 2012; Tabor et al., 2019), mice (Lein et al., 2007), and rhesus macaques (Reveley et al., 2016). We anticipate this resource will contribute to the ascent of adult zebrafish into the upper echelons of model organisms in neuroscience and contribute to our understanding of the evolution, development, and functioning of the vertebrate central nervous system.

Acknowledgments

We thank Maria Palazzolo and Kailyn Fields for help with preparing files associated with the atlas. We thank Angela Morley, Alan Ng, Monica Yu, and Hillary Winstanley for excellent care of the zebrafish, and we thank Tod Thiele for helpful comments on the manuscript. This work was supported by the Human Frontiers Science Program (HFSP; LT000759/2014) , Wayne State University Start-up funds, and the National Institutes of Health (NIH; R35GM142566) to J.W.K, the Canadian Institute for Health Research to P.W.F. (FDN143227). P.W.F is a senior fellow in the Canadian Institute for Advanced Research program in Child and Brain Development. T.M. was supported by the Cognitive and Neurobiological Approaches to Plasticity Center, a Center of Biomedical Research Excellence of the NIH (P20GM113109) and by the HFSP (RGP0016/2019).

472 **Methods**

473 *Subjects*

474 Subjects were AB fish (15-16 weeks of age) of both sexes. Fish were housed in 2 L
475 tanks with 8-12 fish per tank. All fish were bred and raised at the Hospital for Sick Children in
476 high density racks with a 14:10 light/dark cycle (lights on at 8:30) and fed twice daily with
477 *Artemia salina*. All procedures were approved by the Hospital for Sick Children Animal Care and
478 Use Committee.

479

480 *Sample preparation*

481 Zebrafish were euthanized by anesthetizing in 4% tricaine followed by immersion in ice
482 cold water for five minutes. Animals were then decapitated using a razor blade and heads were
483 placed in ice cold PBS for five minutes to let blood drain. Heads were then fixed in 4% PFA
484 overnight after which brains were then carefully dissected into cold PBS and stored at 4 C until
485 processing for iDISCO+. Brains that were damaged during the dissection process were not
486 used for generating the atlas.

487

488 *Tissue staining*

489 Tissue staining and clearing was performed using iDISCO+ (Renier et al., 2016).
490 Samples were first washed three times in PBS at room temperature, followed by dehydration in
491 a series of methanol/water mixtures (an hour each in 20%, 40%, 60%, 80%, 100% methanol).
492 Samples were further washed in 100% methanol, chilled on ice, and then incubated in 5%
493 hydrogen peroxide in methanol overnight at 4 C. The next day, samples were rehydrated in a
494 methanol/water series at room temperature (80%, 60%, 40%, 20% methanol) followed by a PBS
495 wash and two one-hour washes in PTx.2 (PBS with 0.2% TritonX-100). Samples were then

496 washed overnight at 37 C in permeabilization solution (PBS with 0.2% TritonX-100, 0.3 M
497 glycine, 20% DMSO) followed by an overnight incubation at 37 C in blocking solution (PBS with
498 0.2% TritionX-100, 6% normal donkey serum, and 10% DMSO). Samples were then labelled
499 with TO-PRO3 iodide (TO-PRO) (1 night) or primary antibodies (2-3 nights) via incubation at 37
500 C in PTwH (PTx.2 with 10 µg/mL heparin) with 3% donkey serum and 5% DMSO. Samples
501 were then washed at 37 C for one day with five changes of PTwH. Antibody stained samples
502 were followed by incubation with secondary antibodies at 37 C for 2-3 days in PTwH with 3%
503 donkey serum. For samples labelled with TO-PRO, the secondary antibody labelling step was
504 omitted. Following secondary antibody labelling, samples were again washed at 37 C in PTwH
505 for one day with five solution changes.

506

507 *Tissue clearing*

508 Labelled brains were first dehydrated in a series of methanol water mixtures at room
509 temperature (an hour each in 20%, 40%, 60%, 80%, 100% (x2) methanol) and then left
510 overnight in 100% methanol. Samples were then incubated at room temperature in 66%
511 dichloromethane in methanol for three hours followed by two 15-minute washes in
512 dicholormethane. After removal of dichloromethane, samples were incubated and stored in
513 dibenzyl ether until imaging.

514

515 *Imaging*

516 All imaging was done on a LaVision ultramicroscope I. Samples were mounted using an
517 ultraviolet curing resin (adhesive 61 from Norland Optical, Cranbury, NJ) that had a refractive
518 index (1.56) that matched the imaging solution, dibenzyl ether. Images were acquired in the
519 horizontal plane at 4X magnification.

Image processing

Data sets from light sheet imaging were stitched using Fiji's (NIH) extension for Grid Stitching (Preibisch et al., 2009) and converted to a single stack, corresponding to the z-axis. All image processing steps were run on a Linux-workstation with 64 GB of RAM and 12-core Intel processor.

Each stack was converted to a 4 μm isotropic image using custom python code with separate files for the autofluorescence channel and a second for the antibody or TO-PRO channels. These images were resampled to 8 μm isotropic due to system constraints during the image registration stages.

Registration

The TO-PRO and autofluorescence signals were acquired on an initial dataset of 17. To create the initial average, we used image registration to align in a parallel group-wise fashion the TO-PRO images. The variability was expected to be less in the TO-PRO because these images contained more contrast than the autofluorescence images.

The creation of an initial average of the adult zebrafish brain was accomplished using 17 samples with the TO-PRO channel. The process was completed using a 3-step registration process, similar to prior work (Lerch et al., 2011) using the pydpiper pipeline framework (Friedel et al., 2014) and the minctracc registration tool (Collins and Evans, 1997). This involved taking a single sample at random and registering the 17 samples to it using a 6-parameter linear alignment process (LSQ6). This yielded 17 samples in similar orientation to allow a 12-parameter linear registration (LSQ12) to be performed in a pair-wise fashion (each sample is paired with all the other samples, to avoid sample bias) and the final output of these 12-

544 parameter registration was a group average. This represents a linearly registered average adult
545 zebrafish brain. This was then used as the target for non-linear registration with each of the
546 linearly registered 17 TO-PRO samples. This non-linear alignment was repeated successively
547 with smaller step sizes and blurring kernels to allow for an average with minimal bias from any
548 one sample brain. We then took this average and mirrored itself along the long axis of the brain
549 and repeated the registration process described above but instead of using a random brain as
550 the 6-parameter target, we used this mirrored brain. The result of this second pipeline was an
551 average brain where each plane of the brain (coronal, sagittal, horizontal) is parallel with the
552 imaging planes (x,y,z). This final average brain represented the starting point of the atlas. The
553 linear and non-linear transformations created in the registration pipeline were used to resample
554 the 4 μm isotropic TO-PRO and autofluorescence images to the atlas space, yielding an
555 average signal for each channel. The autofluorescence signal was used to register other sample
556 datasets with the atlas because it is common across all datasets.

557 To combine the additional cellular markers to better delineate structures and examine
558 their distribution across the brain, we converted all images and their channels to 4 μm isotropic
559 images as described above. We then converted them to 8 μm isotropic and used the
560 autofluorescence channel for each set to run the above registration pipeline (LSQ6, LSQ12 and
561 non-linear). The initial target was the autofluorescence average created with the TO-PRO
562 dataset described above. Following each registration pipeline, the transformations were used to
563 resample each autofluorescence and cellular marker channel to the atlas with a resolution of 4
564 μm isotropic.

565 To assess registration precision using TO-PRO or autofluorescence images, for each
566 signal we identified 6 landmarks in the atlas, and their corresponding location on 8 different
567 image sets. These points were then brought into atlas space using the transformations from the
568 registration process. We then computed the Euclidean distance between the points in the atlas

image and the transformed images for the TO-PRO and autofluorescence signals. Precision data are presented as mean ± standard deviation unless otherwise indicated.

Segmentation

Segmentation was performed using ITK-SNAP, a freely available software package for working with multimodal medical images that enables side-by-side viewing of 3D images registered into the same anatomical space (Yushkevich et al., 2019). Segmentation was primarily guided by comparing TO-PRO nuclear stained images to the cresyl violet stain of the original atlas (Wullimann et al., 1996). Boundaries of nuclei were often determined using the TO-PRO stain in conjunction with a neuronal marker (HuC/D) and other antibody stains as needed. Terminology largely follows that of the original atlas with the exception of motor nuclei (Mueller et al., 2004) and the telencephalon (Porter and Mueller, 2020).

Figures

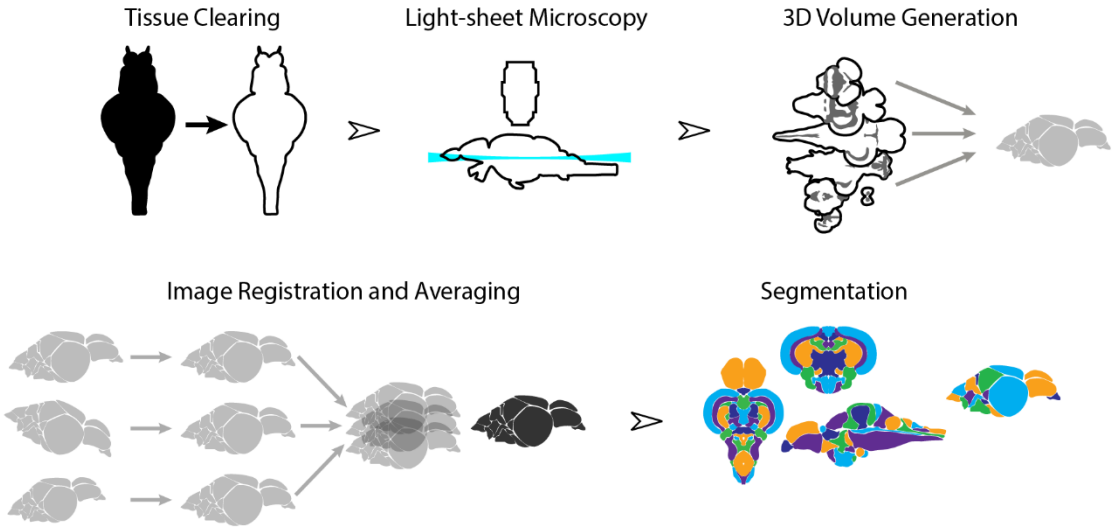

Figure 1. Overview of the strategy for generating AZBA. Dissected brain samples were first subject to staining and tissue clearing. This was followed by whole-mount imaging using light-sheet fluorescence microscopy. Three-dimensional volumes were created from individual image sets, and then registered into the same anatomical space prior to averaging to generate a representative image. Finally, volumes were segmented into over 200 neuroanatomical regions.

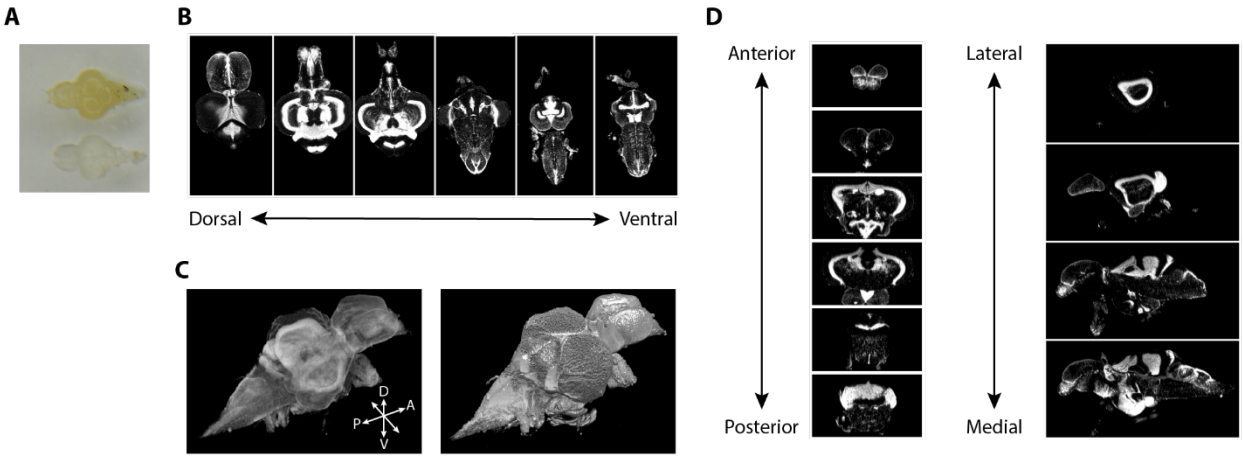

Figure 2. Imaging of nuclear stained tissue-cleared samples. **A)** Image of adult zebrafish brain samples before (top) and after (bottom) clearing using iDISCO+. **B)** Example TO-PRO stained images from a single sample acquired in the horizontal plane during light-sheet imaging. **C)** Three-dimensional volumes generated from a set of light-sheet images from an individual brain visualized using a maximum intensity projection (left), and exterior volume (right). **D)** Coronal (left) and sagittal (right) views of an individual brain generated from a single three-dimensional volume.

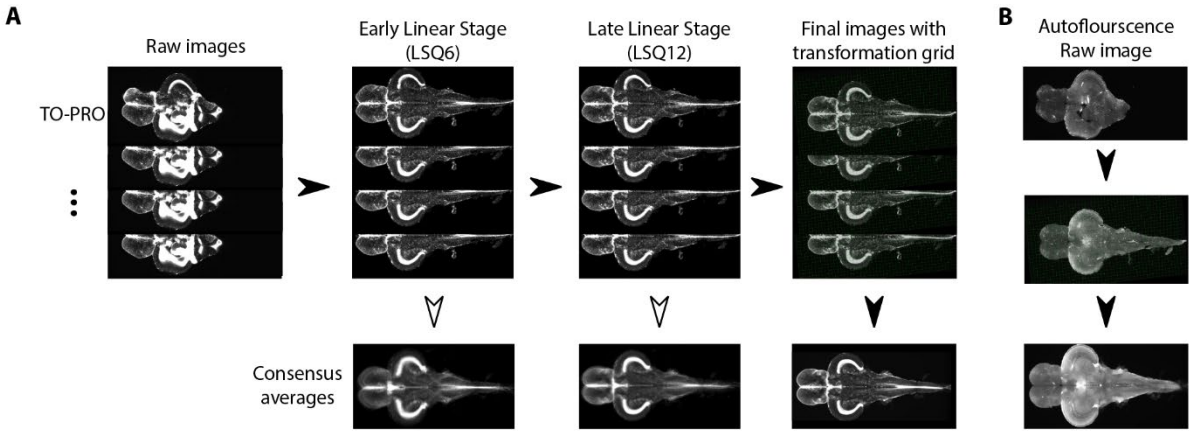

Figure 3. Image registration pipeline. **A)** Raw TO-PRO images from 17 fish were first aligned using linear transformations (LSQ6 and LSQ12) followed by a final non-linear transformation (right). Deformation grids at each stage are overlaid. Consensus average images at each stage of the pipeline are below. **B)** Raw autofluorescence images (top) acquired at the same time as the TO-PRO images were registered into the same space using the transformations derived from TO-PRO registration (middle). Images were then averaged together to generate a corresponding autofluorescence average in the same anatomical space as the TO-PRO images (bottom).

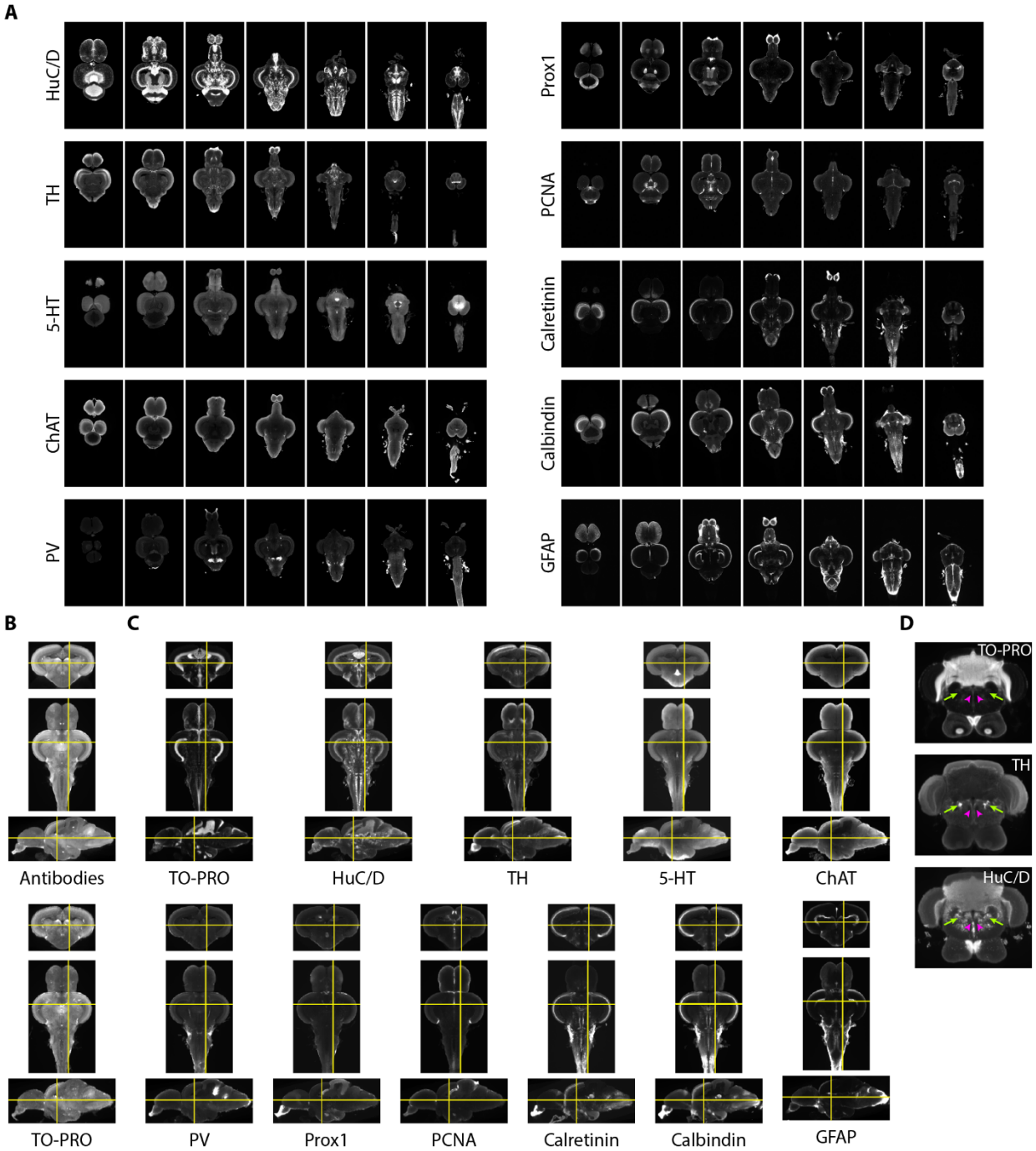

Figure 4. Imaging and registration of antibody stains. **A)** Representative light-sheet images taken in the horizontal plane from individual brains stained with indicated antibodies. **B)** Autofluorescence images acquired during antibody staining (top) were registered into the same space as autofluorescence images acquired during TO-PRO staining (bottom). **C)** Transformations from autofluorescence registration were applied to antibody images to bring antibody stains into the same anatomical space as the TO-PRO stain. Yellow crosshairs are in the same place on each image. **D)** Example of correspondence between TO-PRO and antibody images and how stains can be used to identify the boundaries of specific nuclei (green arrow:

locus coeruleus) and white matter tracts by a lack of staining (pink arrowhead: medial longitudinal fascicle).

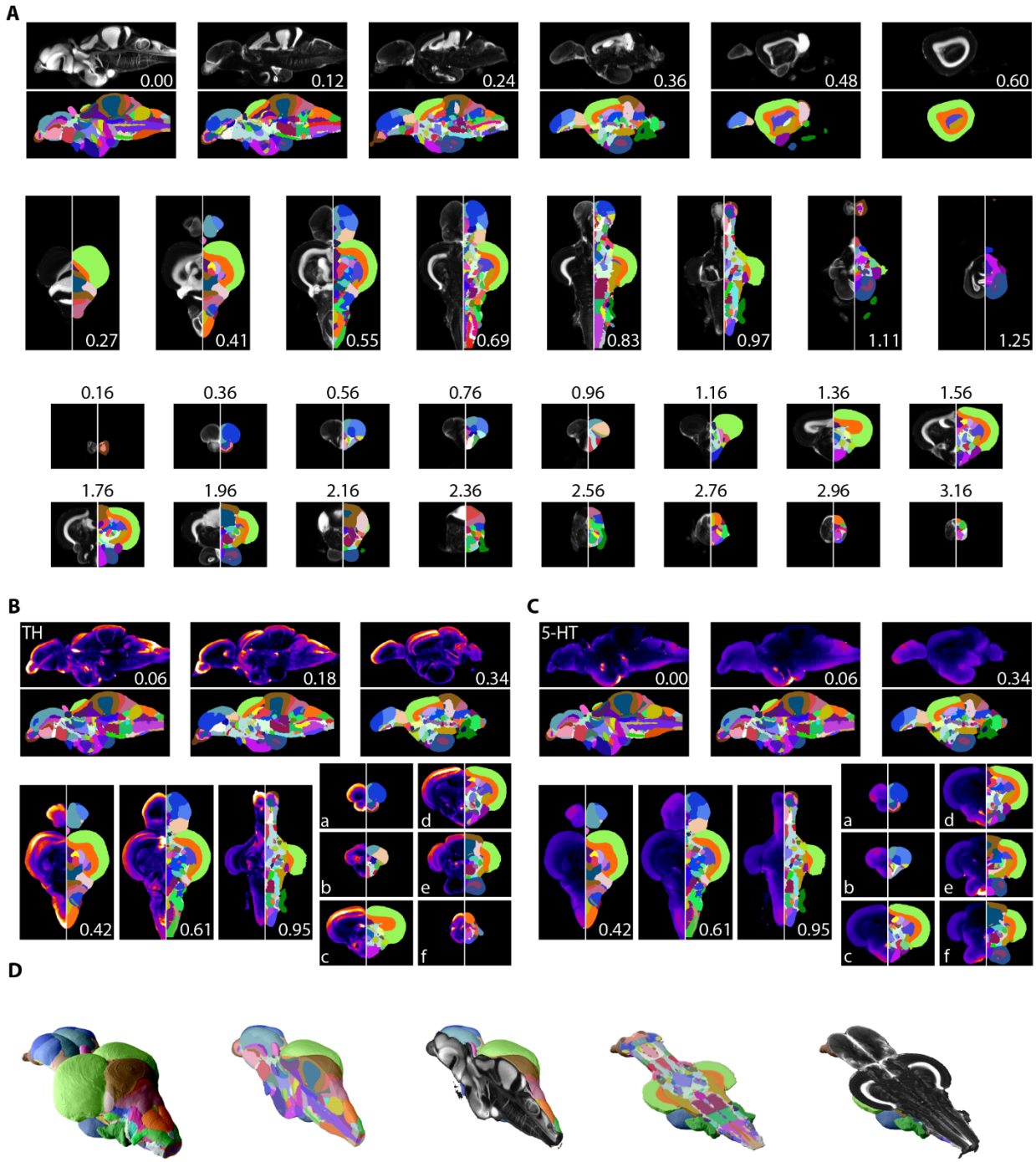

Figure 5. Segmentation of AZBA. **A)** Averaged and registered TO-PRO images alongside the atlas segmentation. For sagittal (top), horizontal (middle), and coronal (bottom) planes numbers are distance (in mm) from the midline, top, and anterior most portion of the brain, respectively. **B and C)** Averaged and registered TH and 5-HT stained images where hotter colors indicate a stronger signal. Numbers same as in (A). Slices in each plane were chosen to show regions

containing high levels of staining (see results for description). **D)** Three-dimensional representation of the segmentation with a sagittal and horizontal cutaway overlaid with TO-PRO the TO-PRO stain of the atlas.

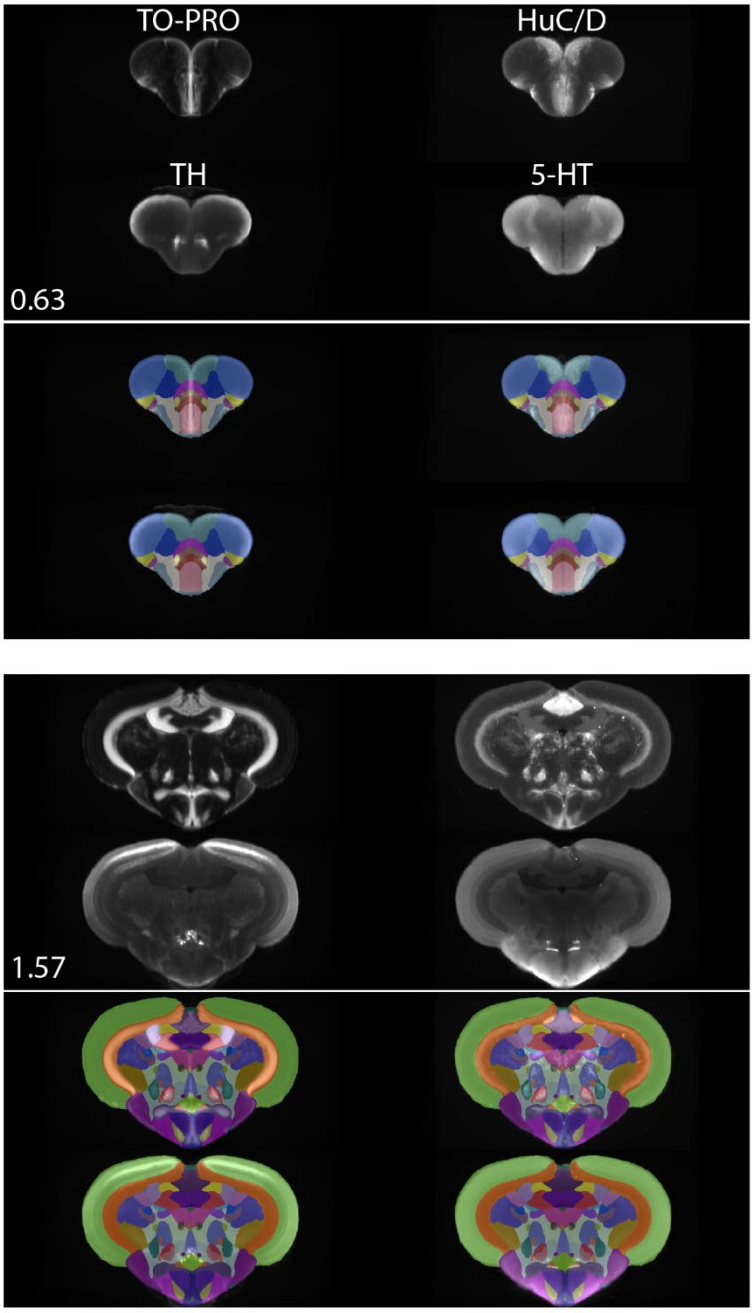

Figure 6. Registered and averaged TO-PRO, HuC/D, TH, and 5-HT images in the coronal plane alongside atlas segmentation at 50% opacity and visualized using ITK-SNAP. Numbers are distance (in mm) from the anterior most portion of the brain.

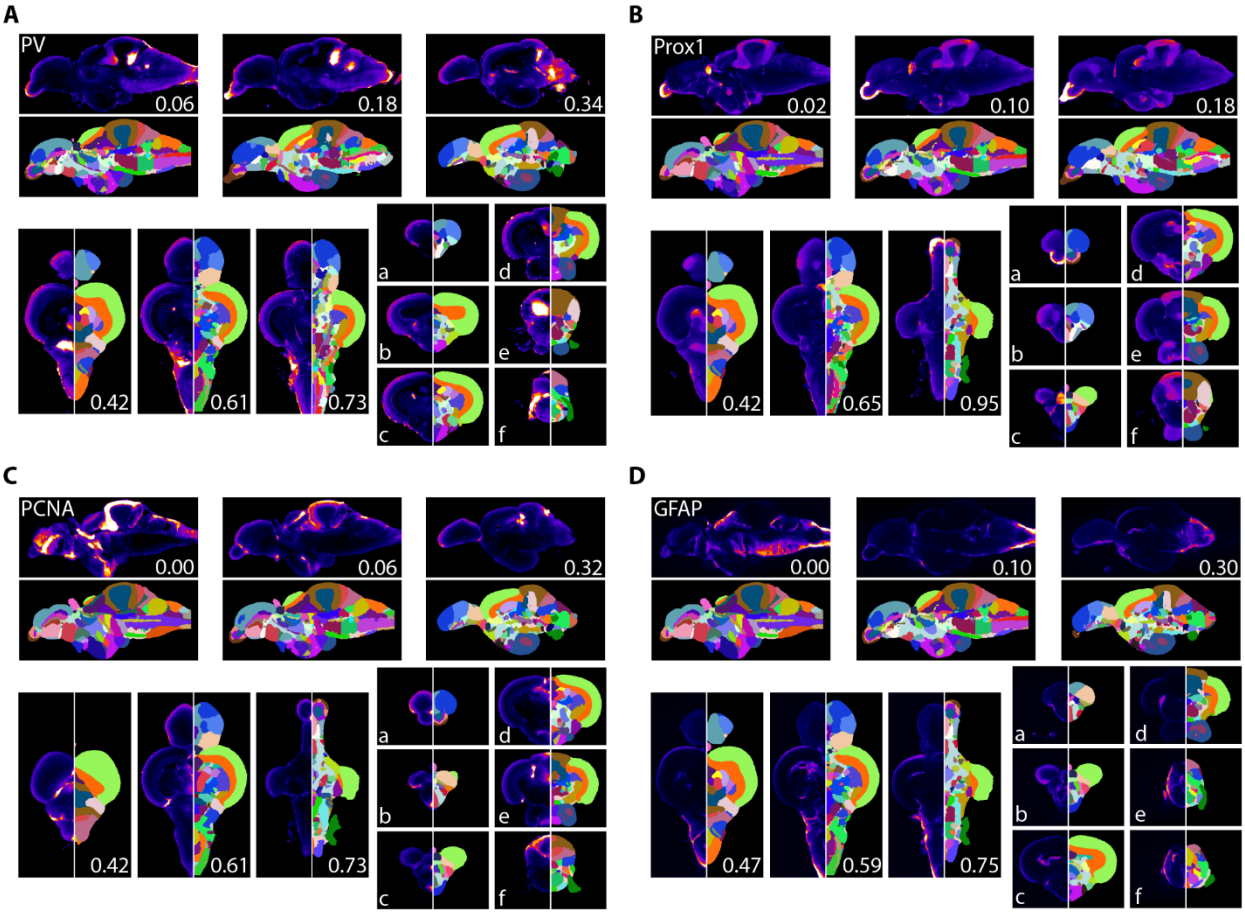

Figure 7. Averaged and registered antibody stains with corresponding segmentation for **A)** PV, **B)** Prox1, **C)** PCNA, and **D)** GFAP where hotter colors indicate greater staining. For sagittal (top) and horizontal (left, bottom) numbers represent distance (in mm) from midline or top of the brain, respectively. Slices for each plane were chosen based on the presence of staining (see results for description).

References

Ahrens MB, Li JM, Orger MB, Robson DN, Schier AF, Engert F, Portugues R. 2012. Brain-wide neuronal dynamics during motor adaptation in zebrafish. *Nature* **485**:471–477. doi:10.1038/nature11057

Ampatzis K, Dermon CR. 2007. Sex differences in adult cell proliferation within the zebrafish (Danio rerio) cerebellum. *Eur J Neurosci* **25**:1030–1040. doi:10.1111/j.1460-9568.2007.05366.x

Ampatzis K, Makantasi P, Dermon CR. 2012. Cell proliferation pattern in adult zebrafish forebrain is sexually dimorphic. *Neuroscience* **226**:367–381. doi:10.1016/j.neuroscience.2012.09.022

Bae YK, Kani S, Shimizu T, Tanabe K, Nojima H, Kimura Y, Higashijima S ichi, Hibi M. 2009. Anatomy of zebrafish cerebellum and screen for mutations affecting its development. *Dev Biol* **330**:406–426. doi:10.1016/j.ydbio.2009.04.013

Bahl A, Engert F. 2020. Neural circuits for evidence accumulation and decision making in larval zebrafish. *Nat Neurosci* **23**:94–102. doi:10.1038/s41593-019-0534-9

Bassett DS, Sporns O. 2017. Network neuroscience. *Nat Neurosci* **20**:353–364. doi:10.1038/nn.4502

Brenowitz EA, Zakon HH. 2015. Emerging from the bottleneck: Benefits of the comparative approach to modern neuroscience. *Trends Neurosci* **38**:273–278. doi:10.1016/j.tins.2015.02.008

Byrd CA, Brunjes PC. 2001. Neurogenesis in the olfactory bulb of adult zebrafish. *Neuroscience* **105**:793–801. doi:10.1016/S0306-4522(01)00215-9

Castro A, Becerra M, Manso MJ, Anadón R. 2006a. Calretinin immunoreactivity in the brain of the zebrafish, Danio rerio: Distribution and comparison with some neuropeptides and neurotransmitter- synthesizing enzymes. II. Midbrain, hindbrain, and rostral spinal cord. *J Comp Neurol* **494**:792–814. doi:10.1002/cne.20843

Castro A, Becerra M, Manso MJ, Anadón R. 2006b. Calretinin immunoreactivity in the brain of the zebrafish, Danio rerio: Distribution and comparison with some neuropeptides and neurotransmitter- synthesizing enzymes. I. Olfactory organ and forebrain. *J Comp Neurol* **494**:435–459. doi:10.1002/cne.20782

Celio MR. 1986. Parvalbumin in most γ-aminobutyric acid-containing neurons of the rat cerebral cortex. *Science (80-)* **231**:995–997. doi:10.1126/science.3945815

Clemente D, Porteros Á, Weruaga E, Alonso JR, Arenzana FJ, Aijón J, Arévalo R. 2004. Cholinergic elements in the zebrafish central nervous system: Histochemical and immunohistochemical analysis. *J Comp Neurol* **474**:75–107. doi:10.1002/cne.20111

Coelho CAO, Ferreira TL, Kramer-Soares JC, Sato JR, Oliveira MGM. 2018. Network supporting contextual fear learning after dorsal hippocampal damage has increased dependence on retrosplenial cortex. *PLOS Comput Biol* **14**:e1006207. doi:10.1371/journal.pcbi.1006207

Collins DL, Evans AC. 1997. Animal: Validation and application of nonlinear registration-based segmentation. *Int J Pattern Recognit Artif Intell* **11**:1271–1294. doi:10.1142/s0218001497000597

787 Doetsch F, García-Verdugo JM, Alvarez-Buylla A. 1997. Cellular composition and three-
788 dimensional organization of the subventricular germinal zone in the adult mammalian brain.
789 *J Neurosci* **17**:5046–5061. doi:10.1523/jneurosci.17-13-05046.1997

790 Dorr AE, Lerch JP, Spring S, Kabani N, Henkelman RM. 2008. High resolution three-
791 dimensional brain atlas using an average magnetic resonance image of 40 adult C57Bl/6J
792 mice. *Neuroimage* **42**:60–69. doi:10.1016/j.neuroimage.2008.03.037

793 Elsir T, Smits A, Lindström MS, Nistér M. 2012. Transcription factor PROX1: Its role in
794 development and cancer. *Cancer Metastasis Rev*. doi:10.1007/s10555-012-9390-8

795 Eng LF, Ghirnikar RS, Lee YL. 2000. Glial Fibrillary Acidic Protein : GFAP-Thirty-One Years (
796 1969 – 2000)* **25**:1439–1451.

797 Friedel M, van Eede MC, Pipitone J, Chakravarty MM, Lerch JP. 2014. Pydpiper: a flexible
798 toolkit for constructing novel registration pipelines. *Front Neuroinform* **8**:67.
799 doi:10.3389/fninf.2014.00067

800 Ganz J, Kaslin J, Freudenreich D, Machate A, Geffarth M, Brand M. 2012. Subdivisions of the
801 adult zebrafish subpallium by molecular marker analysis. *J Comp Neurol* **520**:633–655.
802 doi:10.1002/cne.22757

803 Gerlai R. 2016. Learning and memory in zebrafish (Danio rerio). *Methods Cell Biol* **134**:551–
804 586. doi:10.1016/bs.mcb.2016.02.005

805 Grandel H, Kaslin J, Ganz J, Wenzel I, Brand M. 2006. Neural stem cells and neurogenesis in
806 the adult zebrafish brain: Origin, proliferation dynamics, migration and cell fate. *Dev Biol*
807 **295**:263–277. doi:10.1016/j.ydbio.2006.03.040

808 Idilli AI, Precazzini F, Mione MC, Anelli V. 2017. Zebrafish in Translational Cancer Research:
809 Insight into Leukemia, Melanoma, Glioma and Endocrine Tumor Biology. *Genes (Basel)*
810 **8**:236. doi:10.3390/genes8090236

811 Ito Y, Tanaka H, Okamoto H, Ohshima T. 2010. Characterization of neural stem cells and their
812 progeny in the adult zebrafish optic tectum. *Dev Biol* **342**:26–38.
813 doi:10.1016/j.ydbio.2010.03.008

814 Kaltezioti V, Kouroupi G, Oikonomaki M, Mantouvalou E, Stergiopoulos A, Charonis A, Rohrer
815 H, Matsas R, Politis PK. 2010. Prox1 Regulates the Notch1-Mediated Inhibition of
816 Neurogenesis. *PLoS Biol* **8**:e1000565. doi:10.1371/journal.pbio.1000565

817 Kalueff A V., Gebhardt M, Stewart AM, Cachat JM, Brimmer M, Chawla JS, Craddock C, Kyzar
818 EJ, Roth A, Landsman S, Gaikwad S, Robinson K, Baatrup E, Tierney K, Shamchuk A,
819 Norton W, Miller N, Nicolson T, Braubach O, Gilman CP, Pittman J, Rosemberg DB, Gerlai
820 R, Echevarria D, Lamb E, Neuhauss SCFF, Weng W, Bally-Cuif L, Schneider H,
821 Schneider, and the Zebrafish Neuros H. 2013. Towards a comprehensive catalog of
822 zebrafish behavior 1.0 and beyond. *Zebrafish* **10**:70–86. doi:10.1089/zeb.2012.0861

823 Karalay Ö, Doberauer K, Vadodaria KC, Knobloch M, Berti L, Miquelajauregui A, Schwark M,
824 Jagasia R, Taketo MM, Tarabykin V, Lie DC, Jessberger S. 2011. Prospero-related
825 homeobox 1 gene (Prox1) is regulated by canonical Wnt signaling and has a stage-specific
826 role in adult hippocampal neurogenesis. *Proc Natl Acad Sci U S A* **108**:5807–5812.
827 doi:10.1073/pnas.1013456108

828 Kaslin J, Panula P. 2001. Comparative anatomy of the histaminergic and other aminergic
829 systems in zebrafish (Danio rerio). *J Comp Neurol* **440**:342–377. doi:10.1002/cne.1390

830 Kawakami K, Abe G, Asada T, Asakawa K, Fukuda R, Ito A, Lal P, Mouri N, Muto A, Suster ML,
831 Takakubo H, Urasaki A, Wada H, Yoshida M. 2010. zTrap: zebrafish gene trap and
832 enhancer trap database. *BMC Dev Biol* **10**:105. doi:10.1186/1471-213X-10-105

833 Kenney JW. 2020. Associative and nonassociative learning in adult zebrafishBehavioral and
834 Neural Genetics of Zebrafish. Elsevier. pp. 187–204. doi:10.1016/b978-0-12-817528-
835 6.00012-7

836 Kenney JW, Scott IC, Josselyn SA, Frankland PW. 2017. Contextual fear conditioning in
837 zebrafish. *Learn Mem* **24**:516–523. doi:10.1101/lm.045690.117

838 Kim Y, Venkataraju KU, Pradhan K, Mende C, Taranda J, Turaga SC, Arganda-Carreras I, Ng
839 L, Hawrylycz MJ, Rockland KS, Seung HS, Osten P. 2015. Mapping social behavior-
840 induced brain activation at cellular resolution in the mouse. *Cell Rep* **10**:292–305.
841 doi:10.1016/j.celrep.2014.12.014

842 Kim Y, Yang GR, Pradhan K, Venkataraju KU, Bota M, García del Molino LC, Fitzgerald G, Ram
843 K, He M, Levine JM, Mitra P, Huang ZJ, Wang XJ, Osten P. 2017. Brain-wide Maps Reveal
844 Stereotyped Cell-Type-Based Cortical Architecture and Subcortical Sexual Dimorphism.
845 *Cell* **171**:456-469.e22. doi:10.1016/j.cell.2017.09.020

846 Kizil C, Kaslin J, Kroehne V, Brand M. 2012. Adult neurogenesis and brain regeneration in
847 zebrafish. *Dev Neurobiol* **72**:429–461. doi:10.1002/dneu.20918

848 Klein A, Andersson J, Ardekani BA, Ashburner J, Avants B, Chiang MC, Christensen GE,
849 Collins DL, Gee J, Hellier P, Song JH, Jenkinson M, Lepage C, Rueckert D, Thompson P,
850 Vercauteren T, Woods RP, Mann JJ, Parsey R V. 2009. Evaluation of 14 nonlinear
851 deformation algorithms applied to human brain MRI registration. *Neuroimage* **46**:786–802.
852 doi:10.1016/j.neuroimage.2008.12.037

853 Kramer EE, Steadman PE, Epp JR, Frankland PW, Josselyn SA. 2018. Assessing Individual
854 Neuronal Activity Across the Intact Brain: Using Hybridization Chain Reaction (HCR) to
855 Detect *Arc* mRNA Localized to the Nucleus in Volumes of Cleared Brain Tissue. *Curr*
856 *Protoc Neurosci* **84**:e49. doi:10.1002/cpns.49

857 Kress S, Biechl D, Wullimann MF. 2015. Combinatorial analysis of calcium-binding proteins in
858 larval and adult zebrafish primary olfactory system identifies differential olfactory bulb
859 glomerular projection fields. *Brain Struct Funct* **220**:1951–1970. doi:10.1007/s00429-014-
860 0765-1

861 Kunst M, Laurell E, Mokayes N, Kramer A, Kubo F, Fernandes AM, Förster D, Dal Maschio M,
862 Baier H. 2019. A Cellular-Resolution Atlas of the Larval Zebrafish Brain. *Neuron* **103**:21-
863 38.e5. doi:10.1016/j.neuron.2019.04.034

864 Lal P, Tanabe H, Suster ML, Ailani D, Kotani Y, Muto A, Itoh M, Iwasaki M, Wada H, Yaksi E,
865 Kawakami K. 2018. Identification of a neuronal population in the telencephalon essential
866 for fear conditioning in zebrafish. *BMC Biol* **16**. doi:10.1186/s12915-018-0502-y

867 Lavado A, Oliver G. 2007. Prox1 expression patterns in the developing and adult murine brain.
868 *Dev Dyn* **236**:518–524. doi:10.1002/dvdy.21024

869 Lein ES, Hawrylycz MJ, Ao N, Ayres M, Bensinger A, Bernard A, Boe AF, Boguski MS,
870 Brockway KS, Byrnes EJ, Chen L, Chen TM, Chin MC, Chong J, Crook BE, Czaplinska A,
871 Dang CN, Datta S, Dee NR, Desaki AL, Desta T, Diep E, Dolbeare TA, Donelan MJ, Dong
872 HW, Dougherty JG, Duncan BJ, Ebbert AJ, Eichele G, Estin LK, Faber C, Facer BA, Fields

R, Fischer SR, Fliss TP, Frensley C, Gates SN, Glattfelder KJ, Halverson KR, Hart MR, Hohmann JG, Howell MP, Jeung DP, Johnson RA, Karr PT, Kawal R, Kidney JM, Knapik RH, Kuan CL, Lake JH, Laramee AR, Larsen KD, Lau C, Lemon TA, Liang AJ, Liu Y, Luong LT, Michaels J, Morgan JJ, Morgan RJ, Mortrud MT, Mosqueda NF, Ng LL, Ng R, Orta GJ, Overly CC, Pak TH, Parry SE, Pathak SD, Pearson OC, Puchalski RB, Riley ZL, Rockett HR, Rowland SA, Royall JJ, Ruiz MJ, Sarno NR, Schaffnit K, Shapovalova N V, Sivisay T, Slaughterbeck CR, Smith SC, Smith KA, Smith BI, Sodt AJ, Stewart NN, Stumpf KR, Sunkin SM, Sutram M, Tam A, Teemer CD, Thaller C, Thompson CL, Varnam LR, Visel A, Whitlock RM, Wohnoutka PE, Wolkey CK, Wong VY, Wood M, Yaylaoglu MB, Young RC, Youngstrom BL, Yuan XF, Zhang B, Zwingman TA, Jones AR. 2007. Genome-wide atlas of gene expression in the adult mouse brain. *Nature* **445**:168–176.

Lerch JP, Sled JG, Henkelman RM. 2011. MRI phenotyping of genetically altered mice. *Methods Mol Biol* **711**:349–361. doi:10.1007/978-1-61737-992-5_17

Ma PM. 2003. Catecholaminergic systems in the zebrafish. IV. Organization and projection pattern of dopaminergic neurons in the diencephalon. *J Comp Neurol* **460**:13–37. doi:10.1002/cne.10544

Makantasi P, Dermon CR. 2014. Estradiol treatment decreases cell proliferation in the neurogenic zones of adult female zebrafish (Danio Rerio) brain. *Neuroscience* **277**:306–320. doi:10.1016/j.neuroscience.2014.06.071

Marder E. 2002. Non-mammalian models for studying neural development and function. *Nature* **417**:318–321. doi:10.1038/417318a

McCutcheon V, Park E, Liu E, Sobhebidari P, Tavakkoli J, Wen X-Y, Baker AJ. 2017. A Novel Model of Traumatic Brain Injury in Adult Zebrafish Demonstrates Response to Injury and Treatment Comparable with Mammalian Models. *J Neurotrauma* **34**:1382–1393. doi:10.1089/neu.2016.4497

McLaren DG, Kosmatka KJ, Oakes TR, Kroenke CD, Kohama SG, Matochik JA, Ingram DK, Johnson SC. 2009. A population-average MRI-based atlas collection of the rhesus macaque. *Neuroimage* **45**:52–59. doi:10.1016/j.neuroimage.2008.10.058

Ming G li, Song H. 2011. Adult Neurogenesis in the Mammalian Brain: Significant Answers and Significant Questions. *Neuron*. doi:10.1016/j.neuron.2011.05.001

Mueller T, Dong Z, Berberoglu MA, Guo S. 2011. The dorsal pallium in zebrafish, Danio rerio (Cyprinidae, Teleostei). *Brain Res* **1381**:95–105. doi:10.1016/j.brainres.2010.12.089

Mueller T, Vernier P, Wullimann MF. 2004. The adult central nervous cholinergic system of a neurogenetic model animal, the zebrafish Danio rerio. doi:10.1016/j.brainres.2004.02.073

Nakajo H, Chou MY, Kinoshita M, Appelbaum L, Shimazaki H, Tsuboi T, Okamoto H. 2020. Hunger Potentiates the Habenular Winner Pathway for Social Conflict by Orexin-Promoted Biased Alternative Splicing of the AMPA Receptor Gene. *Cell Rep* **31**:107790. doi:10.1016/j.celrep.2020.107790

Norton WHJ, Folchert A, Bally-Cuif L. 2008. Comparative analysis of serotonin receptor (HTR1A/HTR1B families) and transporter (slc6a4a/b) gene expression in the zebrafish brain. *J Comp Neurol* **511**:521–542. doi:10.1002/cne.21831

Orger MB, de Polavieja GG. 2017. Zebrafish Behavior: Opportunities and Challenges. *Annu Rev Neurosci* **40**:125–147. doi:10.1146/annurev-neuro-071714-033857

Pantoja C, Larsch J, Laurell E, Marquart G, Kunst M, Baier H. 2020. Rapid Effects of Selection on Brain-wide Activity and Behavior. *Curr Biol*. doi:10.1016/j.cub.2020.06.086

Parichy DM. 2015. Advancing biology through a deeper understanding of zebrafish ecology and evolution. *Elife*. doi:10.7554/eLife.05635

Pistocchi A, Gaudenzi G, Carra S, Bresciani E, Del Giacco L, Cotelli F. 2008. Crucial role of zebrafish prox1 in hypothalamic catecholaminergic neurons development. *BMC Dev Biol* **8**:27. doi:10.1186/1471-213X-8-27

Pitrone PG, Schindelin J, Stuyvenberg L, Preibisch S, Weber M, Eliceiri KW, Huisken J, Tomancak P. 2013. OpenSPIM: An open-access light-sheet microscopy platform. *Nat Methods*. doi:10.1038/nmeth.2507

Porter BA, Mueller T. 2020. The Zebrafish Amygdaloid Complex – Functional Ground Plan, Molecular Delineation, and Everted Topology. *Front Neurosci* **14**:608. doi:10.3389/fnins.2020.00608

Preibisch S, Saalfeld S, Tomancak P. 2009. Globally optimal stitching of tiled 3D microscopic image acquisitions. *Bioinforma Appl NOTE* **25**:1463–1465. doi:10.1093/bioinformatics/btp184

Randlett O, Haesemeyer M, Forkin G, Shoenhard H, Schier AF, Engert F, Granato M. 2019. Distributed Plasticity Drives Visual Habituation Learning in Larval Zebrafish. *Curr Biol*. doi:10.1016/j.cub.2019.02.039

Randlett O, Wee CL, Naumann EA, Nnaemeka O, Schoppik D, Fitzgerald JE, Portugues R, Lacoste AMB, Riegler C, Engert F, Schier AF. 2015. Whole-brain activity mapping onto a zebrafish brain atlas. *Nat Methods* **12**:1039–1046. doi:10.1038/nmeth.3581

Renier N, Adams EL, Kirst C, Wu Z, Azevedo R, Kohl J, Autry AE, Kadiri L, Umadevi Venkataraju K, Zhou Y, Wang VX, Tang CY, Olsen O, Dulac C, Osten P, Tessier-Lavigne M. 2016. Mapping of Brain Activity by Automated Volume Analysis of Immediate Early Genes. *Cell* **165**:1789–1802. doi:10.1016/j.cell.2016.05.007

Reveley C, Gruslys A, Ye FQ, Glen D, Samaha J, E. Russ B, Saad Z, K. Seth A, Leopold DA, Saleem KS. 2016. Three-Dimensional Digital Template Atlas of the Macaque Brain. *Cereb Cortex* **27**:4463–4477. doi:10.1093/cercor/bhw248

Reynaud EG, Peychl J, Huisken J, Tomancak P. 2014. Guide to light-sheet microscopy for adventurous biologists, Nature Publishing Group. doi:10.1038/nmeth.3222

Richardson DS, Lichtman JW. 2015. Clarifying Tissue Clearing. *Cell*. doi:10.1016/j.cell.2015.06.067

Rink E, Wullimann MF. 2001. The teleostean (zebrafish) dopaminergic system ascending to the subpallium (striatum) is located in the basal diencephalon (posterior tuberculum). *Brain Res* **889**:316–330. doi:10.1016/S0006-8993(00)03174-7

Ronneberger O, Liu K, Rath M, Rue D, Mueller T, Skibbe H, Drayer B, Schmidt T, Filippi A, Nitschke R, Brox T, Burkhardt H, Driever W. 2012. ViBE-Z: A framework for 3D virtual colocalization analysis in zebrafish larval brains. *Nat Methods* **9**:735–742. doi:10.1038/nmeth.2076

Sakai C, Ijaz S, Hoffman EJ. 2018. Zebrafish Models of Neurodevelopmental Disorders: Past, Present, and Future. *Front Mol Neurosci*. doi:10.3389/fnmol.2018.00294

Schmidt H. 2012. Three functional facets of calbindin D-28k. *Front Mol Neurosci* **5**:25. doi:10.3389/fnmol.2012.00025

Steadman PE, Ellegood J, Szulc KU, Turnbull DH, Joyner AL, Henkelman RM, Lerch JP. 2014. Genetic effects on cerebellar structure across mouse models of autism using a magnetic resonance imaging atlas. *Autism Res* **7**:124–137. doi:10.1002/aur.1344

Tabor KM, Marquart GD, Hurt C, Smith TS, Geoca AK, Bhandiwad AA, Subedi A, Sinclair JL, Rose HM, Polys NF, Burgess HA. 2019. Brain-wide cellular resolution imaging of cre transgenic zebrafish lines for functional circuit-mapping. *Elife* **8**. doi:10.7554/eLife.42687

Ullmann JFP, Cowin G, Kurniawan ND, Collin SP. 2010. A three-dimensional digital atlas of the zebrafish brain. *Neuroimage* **51**:76–82. doi:10.1016/j.neuroimage.2010.01.086

Vetere G, Kenney JW, Tran LM, Xia F, Steadman PE, Parkinson J, Josselyn SA, Frankland PW. 2017. Chemogenetic Interrogation of a Brain-wide Fear Memory Network in Mice. *Neuron* **94**:363-374.e4. doi:10.1016/j.neuron.2017.03.037

von Krogh K, Sørensen C, Nilsson GE, Øverli Ø. 2010. Forebrain cell proliferation, behavior, and physiology of zebrafish, Danio rerio, kept in enriched or barren environments. *Physiol Behav* **101**:32–39. doi:10.1016/j.physbeh.2010.04.003

von Trotha JW, Vernier P, Bally-Cuif L. 2014. Emotions and motivated behavior converge on an amygdala-like structure in the zebrafish. *Eur J Neurosci* **40**:3302–3315. doi:10.1111/ejn.12692

Wang Q, Ding SL, Li Y, Royall J, Feng D, Lesnar P, Graddis N, Naeemi M, Facer B, Ho A, Dolbeare T, Blanchard B, Dee N, Wakeman W, Hirokawa KE, Szafer A, Sunkin SM, Oh SW, Bernard A, Phillips JW, Hawrylycz M, Koch C, Zeng H, Harris JA, Ng L. 2020. The Allen Mouse Brain Common Coordinate Framework: A 3D Reference Atlas. *Cell* **181**:936-953.e20. doi:10.1016/j.cell.2020.04.007

Wheeler AL, Teixeira CM, Wang AH, Xiong X, Kovacevic N, Lerch JP, McIntosh AR, Parkinson J, Frankland PW. 2013. Identification of a functional connectome for long-term fear memory in mice. *PLoS Comput Biol* **9**:e1002853.

Wulliman MF, Rupp B, Reichert H. 1996. Neuroanatomy of the zebrafish brain: a topological atlas. Birkhäuser.

Wullimann MF, Puelles L. 1999. Postembryonic neural proliferation in the zebrafish forebrain and its relationship to prosomeric domains. *Anat Embryol (Berl)* **199**:329–348. doi:10.1007/s004290050232

Wullimann MF, Rupp B, Reichert H. 1996. Neuroanatomy of the Zebrafish Brain: A Topological Atlas, Neuroanatomy of the Zebrafish Brain. Birkhäuser Verlag, Basel. doi:10.1007/978-3-0348-8979-7

Xi Y, Noble S, Ekker M. 2011. Modeling neurodegeneration in zebrafish. *Curr Neurol Neurosci Rep* **11**:274–282. doi:10.1007/s11910-011-0182-2

Yamamoto K, Ruuskanen JO, Wullimann MF, Vernier P. 2010. Two tyrosine hydroxylase genes in vertebrates. New dopaminergic territories revealed in the zebrafish brain. *Mol Cell Neurosci* **43**:394–402. doi:10.1016/j.mcn.2010.01.006

Yartsev MM. 2017. The emperor's new wardrobe: Rebalancing diversity of animal models in neuroscience research. *Science (80-)* **358**:466–469. doi:10.1126/science.aan8865

Yushkevich PA, Pashchinskiy A, Oguz I, Mohan S, Schmitt JE, Stein JM, Zukić D, Vicory J, McCormick M, Yushkevich N, Schwartz N, Gao Y, Gerig G. 2019. User-Guided Segmentation of Multi-modality Medical Imaging Datasets with ITK-SNAP. *Neuroinformatics* **17**:83–102. doi:10.1007/s12021-018-9385-x

1031 **Supplemental Information**

1032 Table S1: Stains

Label	Source	Cat #	Concentration
TO-PRO3 Iodide	Invitrogen	T3605	1:10,000
Primary Antibodies			
Anti-TH	Aves	TYH	1:200
Anti-GFAP	ZIRC	Zrf-1	1:200
Anti-ChAT	Millipore	AB144	1:400
Anti-5-HT	Sigma	S5545	1:100
Anti-Calbindin	SWANT	CB38a	1:200
Anti-Calretinin	SWANT	6B3	1:400
Anti-PCNA	Dako	M0879	1:1000
Anti-HuCD	Invitrogen	A-21271	3.75 µg/mL
Anti-Prox1	Millipore	AB5475	1:400
Anti-Parvalbumin	SWANT	PV27	1:400
Secondary Antibodies			
Donkey anti-mouse Alexa Flour 647	Invitrogen	A31571	1:200
Donkey anti-rabbit Alexa Flour 647	Invitrogen	A31573	1:200
Donkey anti-goat Alexa Flour 647	Invitrogen	A21447	1:200
Goat anti-chicken Alexa Flour 633	Invitrogen	A21103	1:200

1033

1034

1035

1036

1037

1038

1039

1040

1041

1042

1043

1044

1045

1046

1047

1048

1049

Table S2: Brain region abbreviations, full names, and colors

Abbreviation	Full name	Color
A	anterior thalamic nucleus	
AC	anterior cerebellar tract	
ALLN	anterior lateral line nerves	
AON	anterior octaval nucleus	
APN	accessory pretectal nucleus	
ATN	anterior tuberal nucleus	
BSTa	bed nucleus of the stria terminalis, anterior division	
BSTm	bed nucleus of the stria terminalis, medial division	
BSTpd	bed nucleus of the stria terminalis, posterior division	
C	central canal	
Cans	ansulate commissure	
Cantd	anterior commissure, dorsal part	
Cantv	anterior commissure, ventral part	
CC	cerebellar crest	
CCe-g	cerebellar corpus, granular layer	
CCe-m	cerebellar corpus, molecular layer	
Ccer	cerebellar commissure	
Cgus	commissure of the secondary gustatory nuclei	
Chab	habenular commissure	
Chor	horizontal commissure	
CIL	central nucleus of the inferior lobe	
Cinf	commissura infima of Haller	
CM	mammillary body	
CO/OT	optic chiasm / optic tract	
CON	caudal octavolateralis nucleus	
CP	central posterior thalamic nucleus	
CPN	central pretectal nucleus	
CPop	supraoptic commissure	
Cpost	posterior commissure	
Ctec	tectal commissure	
Ctub	commissure of the posterior tuberculum	
Cven	ventral rhombencephalic commissure	
DAO	dorsal accessory optic nucleus	
Dc	central zone of dorsal telencephalon area	
DH	dorsal horn	
DIL	diffuse nucleus of the inferior lobe	
DiV	diencephalic ventricle	
DIV	trochlear decussation	

Dl	lateral zone of the dorsal telencephalon
Dm	medial zone of dorsal telencephalon
DON	descending octaval nucleus
DOT	dorsomedial optic tract
Dp	posterior zone of dorsal telencephalon area
DP	dorsal posterior thalamic nucleus
DR	dorsal root
DTN	dorsal tegmental nucleus
DV	descending trigeminal root
E	epiphysis
ECL	external cellular layer of olfactory bulb
EG	granular eminence
EmTl	lateral thalamic eminence
EmTm	medial thalamic eminence
EmTr	rostral thalamic eminence
ENd	entopeduncular nucleus, dorsal part
ENv	entopeduncular nucleus, ventral part
EW	Edinger-Westphal nucleus
Flv	ventral part of lateral funiculus
FR	habenulo-interpeduncular tract
Fv	ventral funiculus
GC	central gray
GL	glomerular layer of olfactory bulb
Had	dorsal habenular nucleus
Hav	ventral habenular nucleus
Hc	caudal zone of periventricular hypothalamus
Hd	dorsal zone of periventricular hypothalamus
Hv	ventral zone of periventricular hypothalamus
I (thalamus)	Intermediate thalamic nucleus
IAF	inner arcuate fibers
ICL	internal cellular layer of olfactory bulb
IMRF	intermediate reticular formation
IN	Intermediate nucleus
IO	inferior olive
IR	inferior raphe
IRF	inferior reticular formation
LC	locus coeruleus
LCa	caudal lobe of cerebellum
LFB	lateral forebrain bundle
LH	lateral hypothalamic nucleus
LLF	lateral longitudinal fascicle

LOT	lateral olfactory tract
LR	lateral recess of diencephalic ventricle
LRN	lateral reticular nucleus
MAC	Mauthner cell
MaON	magnocellular octaval nucleus
MFB	medial forebrain bundle
MFN	medial funicular nucleus
MLF	medial longitudinal fascicle
MON	medial octavolateralis nucleus
MOT	medial olfactory tract
NC	commissural nucleus of Cajal
NDV	nucleus of the descending trigeminal root
NI	isthmic nucleus
NIn	interpeduncular nucleus
NLL	nucleus of the lateral lemniscus
nLOT-a	nucleus of the lateral olfactory tract, anterior part
nLOT-i	nucleus of the lateral olfactory tract, intermediate part
nLOT-p	nucleus of the lateral olfactory tract, posterior part
NLV	nucleus lateralis valvulae
NMLF	nucleus of the medial longitudinal fascicle
NR	red nucleus
OENc	octavolateralis efferent neurons, caudal part
OENr	octavolateralis efferent neurons, rostral part
P	posterior thalamic nucleus
PC	posterior cerebellar tract
PCN	paracommissural nucleus
PGa	anterior preglomerular nucleus
PGc	caudal preglomerular nucleus
PGl	lateral preglomerular nucleus
PGm	medial preglomerular nucleus
PGZ	periventricular gray zone of optic tectum
PL	perilemniscal nucleus
PLLN	posterior lateral line nerve
PM	magnocellular preoptic nucleus
PMg	gigantocellular part of magnocellular preoptic nucleus
PO	posterior pretectal nucleus
POF	primary olfactory fiber layer
PON	posterior octaval nucleus
PPa	parvocellular preoptic nucleus, anterior part
PPd	periventricular pretectal nucleus, dorsal part
PPp	parvocellular preoptic nucleus, posterior part

PPv	periventricular pretectal nucleus, ventral part
PR	posterior recess of diencephalic ventricle
PSm	magnocellular superficial pretectal nucleus
PSp	parvocellular superficial pretectal nucleus
PTN	posterior tuberal nucleus
PVO	paraventricular organ
R	rostrolateral nucleus
RT	rostral tegmental nucleus
RV	rhombencephalic ventricle
SC	suprachiasmatic nucleus
SCO	subcommissural organ
SD	dorsal sac
SG	subglomerular nucleus
SGN	secondary gustatory nucleus
SGT	secondary gustatory tract
SO	secondary octaval population
SR	superior raphe
SRF	superior reticular formation
SRN	superior reticular nucleus
T	tangential nucleus
TBS	bulbo-spinal tract
TelV	telencephalic ventricles
TeO	optic tectum
TeV	tectal ventricle
TGN	tertiary gustatory nucleus
TL	longitudinal torus
TLa	lateral torus
TMCa	anterior mesencephalo-cerebellar tract
TMCp	posterior mesencephalo-cerebellar tract
TPM	pretecto-mammillary tract
TPp	periventricular nucleus of posterior tuberculum
TSc	central nucleus of semicircular torus
TSvl	ventrolateral nucleus of semicircular torus
TTB	tecto-bulbar tract
TTBc	crossed tecto-bulbar tract
TTBr	uncrossed tecto-bulbar tract
TVS	vestibulo-spinal tract
Val-g	lateral division of valvula cerebelli, granular layer
Val-m	lateral division of valvula cerebelli, molecular layer
Vam-g	medial division of valvula cerebelli, granular layer
Vam-m	medial division of valvula cerebelli, molecular layer

VAO	ventral accessory optic nucleus
Vas	vascular lacuna of area postrema
Vc	central nucleus of ventral telencephalon area
Vd-dd	dorsal zone of ventral telencephalon
Vd-vd	ventral zone of ventral telencephalon
Vdd	dorsal most zone of ventral telencephalon
Vl	lateral nucleus of ventral telencephalon area
VL	ventrolateral thalamic nucleus
VM	ventromedial thalamic nucleus
VOT	ventrolateral optic tract
Vp	postcommissural nucleus of ventral telencephalon area
Vs	supracommissural nucleus of ventral telencephalon area
Vv	ventral nucleus of ventral telencephalon area
ZL	zona limitans
III	oculomotor nerve
IIIm	oculomotor nucleus
IV	trochlear nerve
IVm	trochlear nucleus
V	trigeminal nerve
Vmd	trigeminal motor nucleus, dorsal part
Vmn	mesencephalic nucleus of the trigeminal nerve
Vmv	trigeminal motor nucleus, ventral part
Vmvr	ventral trigeminal motor root
Vsm	primary sensory trigeminal nucleus
Vsr	sensory root of the trigeminal nerve
VImc	caudal abducens nerve motor nucleus
VImr	rostral abducens nerve motor nucleus
VIILo	facial lobe
VIIm	facial motor nucleus
VIImr	facial motor root
VIIs	sensory root of the facial nerve
VIII	octaval nerve
IXLo	glossopharyngeal lobe
IXm	glossopharyngeal nerve motor nucleus
X	vagal nerve
XLo	vagal lobe
Xm	vagal motor nucleus
UnkD	unknown diencephalon
UnkMS	unknown mesencephalon
UnkR	unknown rhombencephalon
UnkSC	unknown spinal cord

UnkVT	unknown ventral telencephalon

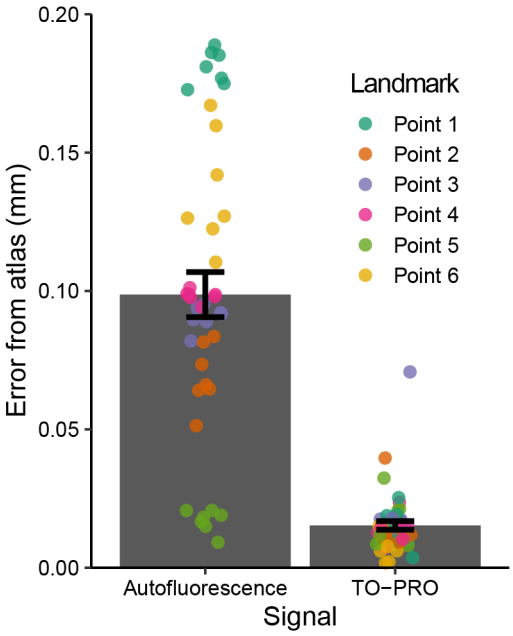

Figure S1. Registration precision between six different landmarks in the autofluorescence and TO-PRO images and their respective atlas images. Data are mean ± SEM.

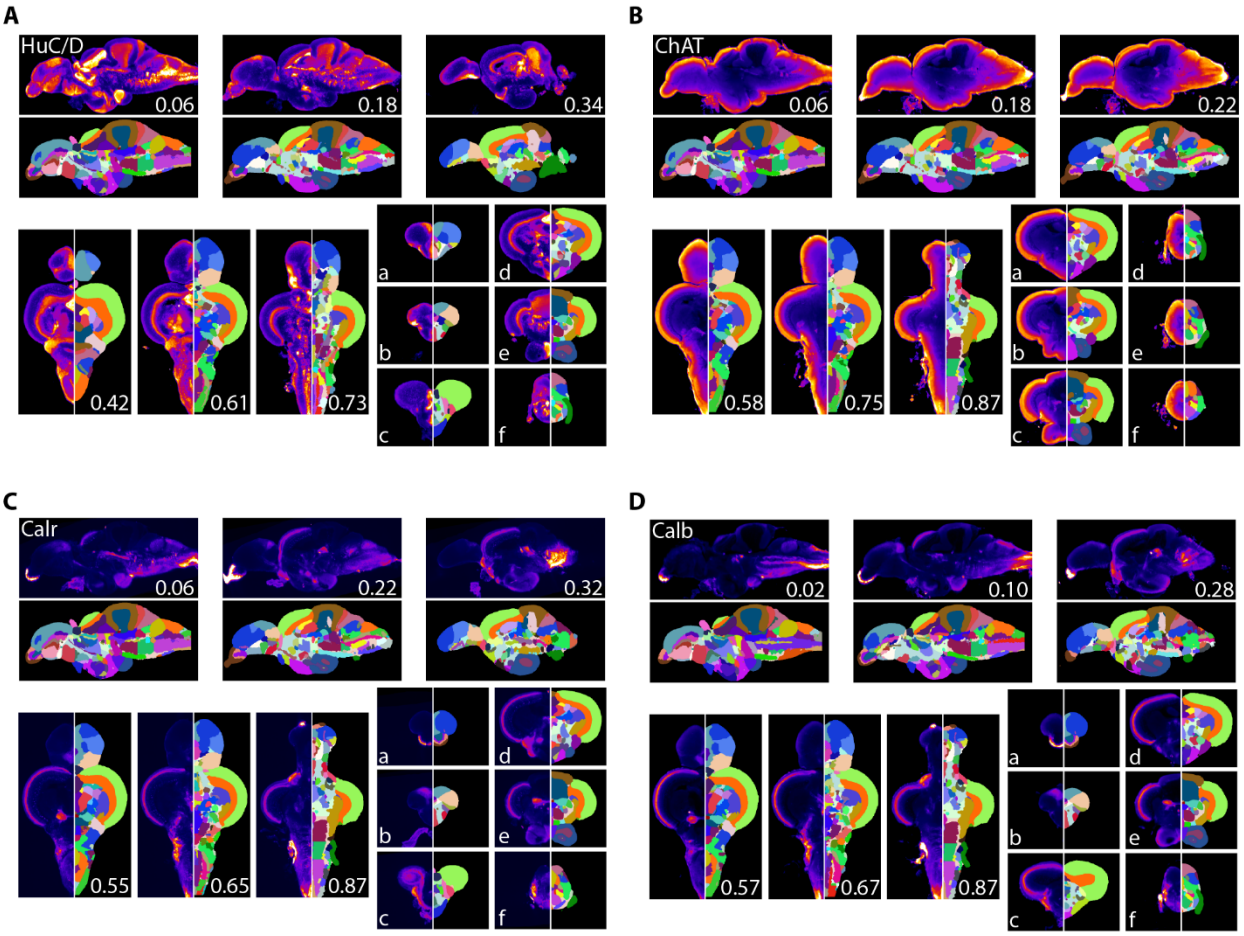

Figure S2. Averaged and registered antibody stains with corresponding segmentation for **A)** HuC/D, **B)** ChAT, **C)** Calretinin (Calr), and **D)** Calbindin (Calb) where hotter colors indicate greater staining. For sagittal (top) and horizontal (left, bottom) numbers represent distance (in mm) from midline or top of the brain, respectively. Slices for each plane were chosen based on the presence of staining (see results for description).

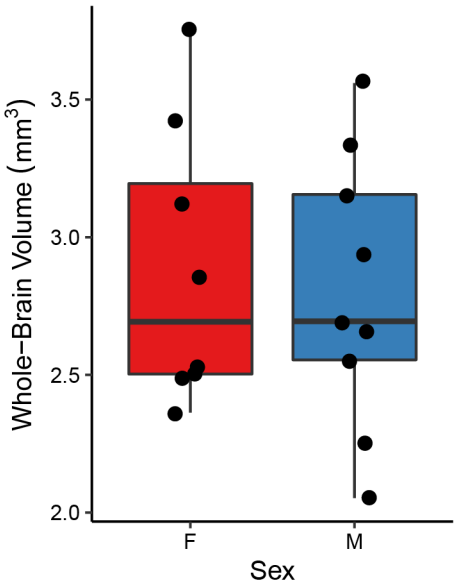

Figure S3. Whole-brain volumes of female and male fish used in the TO-PRO registration.

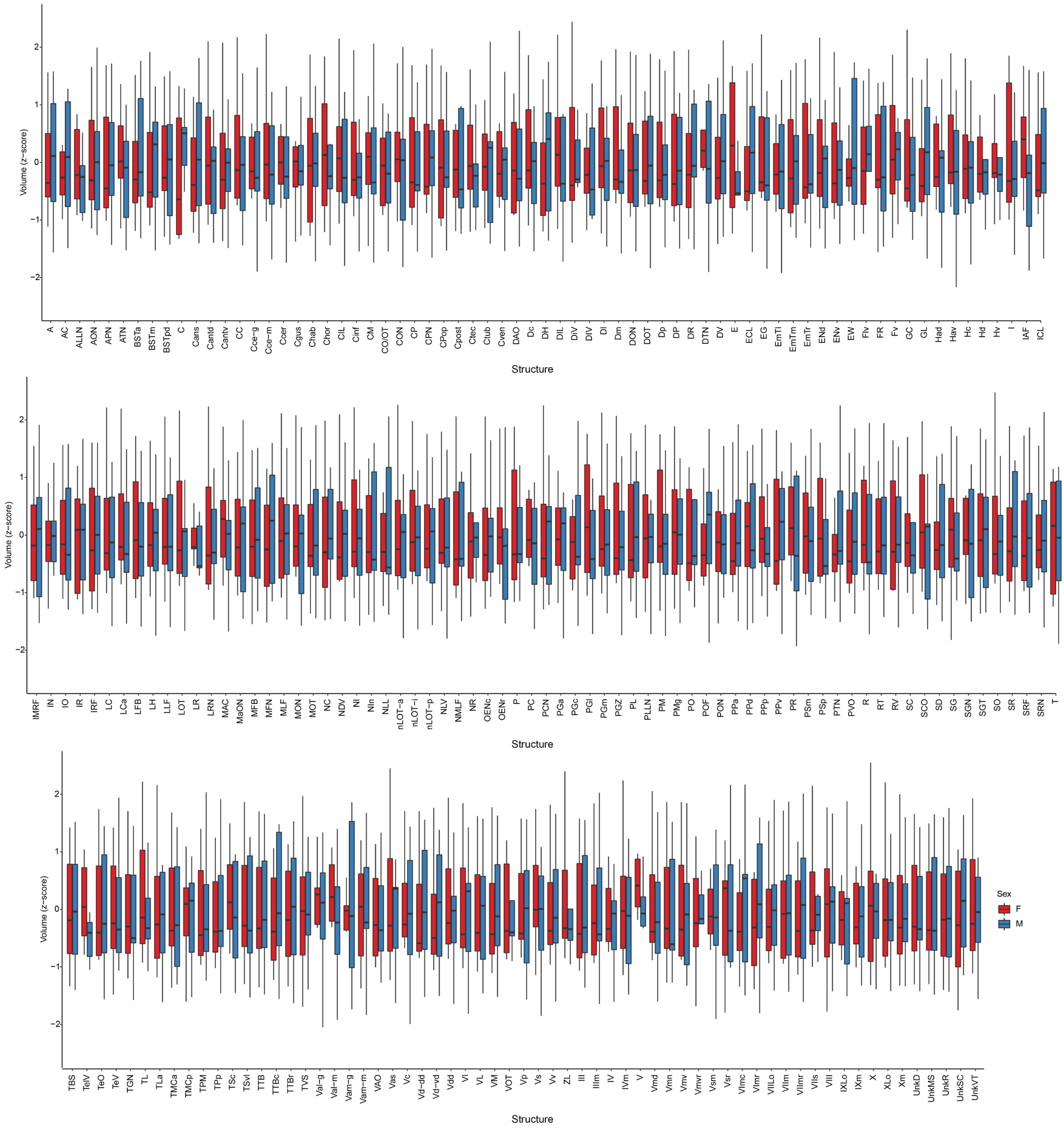

1163 *Figure S4.* Brain structure volumes of female and male fish used in the TO-PRO registration. For abbreviation definitions see Table S2.